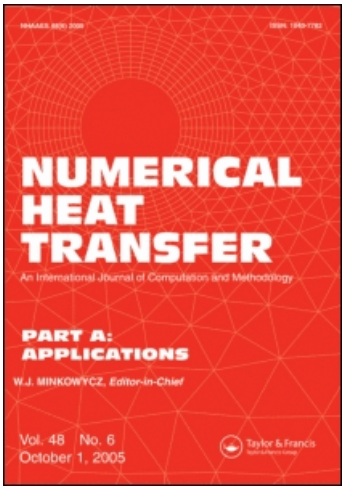

Numerical Heat Transfer, Part A: Applications
Publication details, including instructions for authors and subscription information:
http://www.informaworld.com/smpp/title~content=t713657973

Numerical Modeling of Cold Weld Formation and Improvement in Gmaw of Aluminum Alloys

H. Guo[a]; J. Hu[b]; H. L. Tsai[a]
[a] Department of Mechanical and Aerospace Engineering, Missouri University of Science and Technology (formerly University of Missouri-Rolla), Rolla, Missouri, USA [b] Department of Mechanical Engineering, University of Bridgeport, Bridgeport, Connecticut, USA

Online publication date: 10 March 2010

To cite this Article Guo, H. , Hu, J. and Tsai, H. L.(2010) 'Numerical Modeling of Cold Weld Formation and Improvement in Gmaw of Aluminum Alloys', Numerical Heat Transfer, Part A: Applications, 57: 6, 392 — 414
To link to this Article: DOI: 10.1080/10407781003613349
URL: http://dx.doi.org/10.1080/10407781003613349

Numerical Heat Transfer, Part A, 57: 392–414, 2010

ISSN: 1040-7782 print/1521-0634 online
DOI: 10.1080/10407781003613349

Taylor & Francis
Taylor & Francis Group

NUMERICAL MODELING OF COLD WELD FORMATION AND IMPROVEMENT IN GMAW OF ALUMINUM ALLOYS

H. Guo[1], J. Hu[2], and H. L. Tsai[1]

[1]*Department of Mechanical and Aerospace Engineering, Missouri University of Science and Technology (formerly University of Missouri-Rolla), Rolla, Missouri, USA*

[2]*Department of Mechanical Engineering, University of Bridgeport, Bridgeport, Connecticut, USA*

Both mathematical modeling and experiments have been conducted on the formation of cold weld in gas metal arc welding (GMAW) of aluminum alloy 6005-T4. Transient weld pool shape and the distributions of temperature and velocity were calculated by a three-dimensional numerical model. The final weld bead shape and dimensions and peak temperature in the heat-affected zone (HAZ) were obtained. Three techniques were proposed to input more energy at the initial state of welding to improve weld bead penetration. Both the simulation and the experimental results show significantly improved weld bead penetration at the start of welding.

1. INTRODUCTION

Gas metal arc welding (GMAW) is one of the most popular welding methods in the industry. It uses a metal wire as a combined electrode and filler metal in a plasma arc and inert shielding gas. In the auto industry, due to the demands for a lower environmental impact through improved fuel efficiency by weight reduction, more automobile body structures are being manufactured with aluminum instead of steel. One feature of these welds is that they are much shorter than normal welds. They are usually less than 10 cm in length, and many are only around 3 or 4 cm. Therefore, the beginning end (cold weld) makes up a large portion of short welds (Figure 1). In the cold weld, the work piece is in a relatively cold state when the welding begins and is heated up gradually during the process. There is not much pre-heating effect by the welding arc compared with a normal weld. Hence, a lack of penetration always occurs at a cold weld and the mechanical performance of the weld joint is vastly lowered.

In addition, unlike the middle portion of a long weld where the welding process is in a quasi-steady state, the energy, mass, and momentum transfer varies sharply from moment to moment in a cold weld; thus, creating very unsteady temperature

Received 3 July 2009; accepted 15 December 2009.

Address correspondence to J. Hu, Department of Mechanical Engineering, University of Bridgeport, Bridgeport, CT 06604, USA. E-mail: jjhu@bridgeport.edu

NOMENCLATURE

$\vec{B}$	magnetic induction vector	$\vec{V}$	velocity vector
c	specific heat	$\vec{V}_r$	relative velocity vector between the liquid phase and solid phase.
C	inertial coefficient		
f	mass fraction	w	velocity in z direction
F	volume of fluid function	W	melt mass evaporation rate
g	gravitational acceleration	β_T	thermal expansion coefficient
h	enthalpy	ε	surface radiation emissivity
h_c	convective heat transfer coefficient	γ	surface tension coefficient
H_v	latent heat of vaporization	κ	free surface curvature
I	welding current	μ	dynamic viscosity
$\vec{J}$	current density vector	η	arc thermal efficiency
k	thermal conductivity	η_d	ratio of droplet thermal energy to the total arc energy
K	permeability function		
$\vec{n}$	normal vector to the local surface	σ	Stefan-Boltzmann constant
p	pressure	ρ	density
p_v	vapor pressure or any other applied external pressure	σ_p	arc pressure distribution parameter
		σ_q	arc heat flux distribution parameter
$P_{\max}$	maximum arc pressure at the arc center	$\tau_{\vec{s}}$	Marangoni shear stress
r-z	cylindrical coordinate system		
$\vec{s}$	local surface tangential vector	**Subscripts**	
t	time	0	initial condition
T	temperature	d	droplet
u	velocity in x, direction	l	liquid phase
u_w	arc voltage	m	melting point of aluminum
v	velocity in y, direction	s	solid phase

and fluid flow fields, leading to increased weld defects. Porosity is a major defect in the cold weld. Aluminum is very sensitive to hydrogen, which plays an important role in the formation of porosity [1]. Hydrogen is entrapped and creates porosity in the weld metal due to its sudden and significant solubility drop during the solidification stage [2–7]. In the cold weld, the liquid metal solidifies quickly since the temperature of the metal is still low, leading to more porosity. An important source of the hydrogen is the moisture in the shielding gas. To prevent hydrogen-induced porosity, the shielding gas should contain the lowest possible moisture. Porosity is

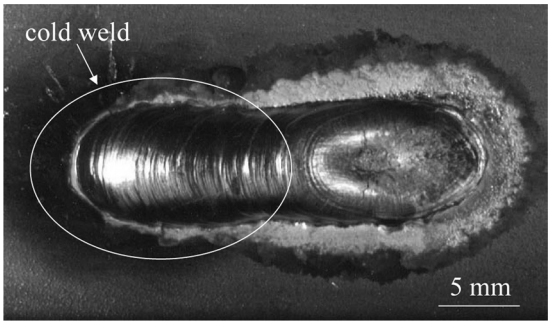

Figure 1. A cold weld.

usually a result of the lack of preparation and cleaning prior to the welding [8]. The oxides on the surface of the weld wire can hold moisture that will produce porosity [9, 10]. Therefore, the weld area and weld wire should be thoroughly cleaned before welding. Removal of oxide is also necessary to help reduce weld porosity [1, 3]. Flow status of shielding gas is another factor. To prevent the formation of porosity, the flow of shielding gas should be steady and not too high or too low [8] so a laminar flow can be established, which provides better protection.

Numerous studies have been carried out on the welding process, but few have been done on the improvement of the penetration for cold welds, although some studies have been performed to improve the properties of the cold weld in GTAW. Tong found that the small penetration at the welding start point is due to the lack of preheating [11]. A "Starting—Delay" technique was used for starting the gas tungsten welding process in high-purity aluminum, which provided the additional initial heating to the weldment [11]. A 60% increase of penetration depth was obtained at the beginning of the weldment [11]. However, no detailed analysis has been reported on the starting stage of gas metal arc welding of aluminum alloys.

To get a better understanding of the gas metal arc welding (GMAW) process of aluminum alloys, both experimental and theoretical research should be carried out. Many theoretical models have been established on the simulation of gas metal arc welding process [12–23]. Among them, references [18, 20–22] developed detailed models on the impingement of filler droplets and weld pool dynamics, and calculated the combined effect of droplet impingement and surface tension. However, all the research efforts were only focused on the quasi-steady state part of the GMAW process, and no theoretical investigation was reported on the starting stage of welding.

The objectives of this project are to obtain a better understanding of the formation mechanism of the cold weld and to find a proper welding approach to improve the weld penetration. The fluid flow and heat transfer were calculated when droplets carry mass, momentum, and thermal energy into the weld pool. The transient deformed weld pool surface was handled by the VOF technique [24], and the fusion and solidification in the liquid region, the mushy zone, and the solid region were handled by continuum formulation [25]. In experimental research, bead-on-plate experiments were performed. The welding conditions were recorded and stored in the computer to plug into the mathematical model. Experimental samples were then characterized using metallographic methods including optical microscopy and micro-hardness test.

2. MATHEMATICAL MODEL

A sketch of a moving GMAW system for a plate is shown in Figure 2. The three-dimensional x-y-z coordinate system is fixed to the base metal, with the arc moving in the positive x direction. As the focus of the study is on the weld pool dynamics and weld formation under the droplet impingement, in order to save computational time, the droplet generation and the arc plasma are not calculated. Instead, typical droplet conditions, including size, impinging velocity, temperature, and frequency are assumed. The plasma arc is assumed to have a Gaussian profile.

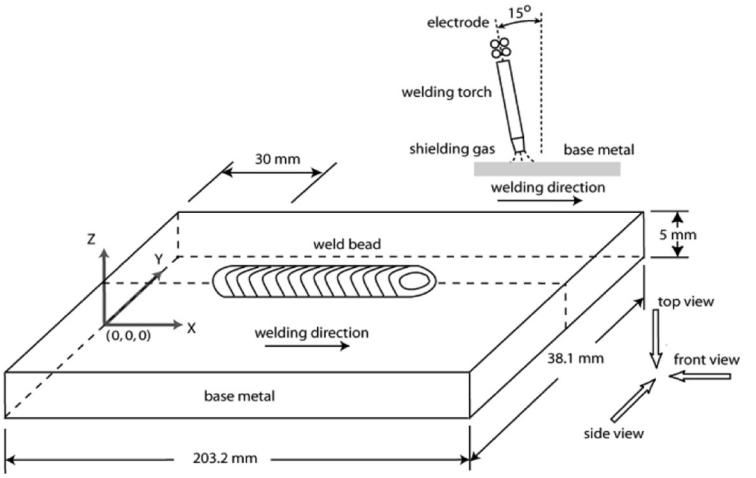

Figure 2. Experimental setup and simulation domain of a GMAW system.

Note, these assumptions should not change the fundamental characteristics of the droplet impinging process and the resulting weld pool dynamics and cold weld formation to be studied in the present study.

2.1. Governing Equations

The differential equations governing the conservation of mass, momentum, and energy based on continuum formulation given by Diao and Tsai [25] were modified and employed in the study. The equations are given below.

Continuity

$$\frac{\partial \rho}{\partial t} + \nabla \cdot \left(\rho \vec{\boldsymbol{V}}\right) = 0 \tag{1}$$

where t is the time, ρ is the density, and $\vec{V}$ is the velocity vector.

Momentum

$$\frac{\partial}{\partial t}(\rho u) + \nabla \cdot \left(\rho \vec{\boldsymbol{V}} u\right) = \nabla \cdot \left(\mu_l \frac{\rho}{\rho_l} \nabla u\right) - \frac{\partial p}{\partial x} - \frac{\mu_l}{K} \frac{\rho}{\rho_l}(u - u_s) - \frac{C\rho^2}{K^{1/2}\rho_l}|u - u_s|(u - u_s) - \nabla \cdot \left(\rho f_s f \vec{\boldsymbol{V}}_r u_r\right) + \vec{\boldsymbol{J}} \times \vec{\boldsymbol{B}}|_x \tag{2}$$

$$\frac{\partial}{\partial t}(\rho v) + \nabla \cdot (\rho \vec{\boldsymbol{V}} v) = \nabla \cdot \left(\mu_l \frac{\rho}{\rho_l} \nabla v\right) - \frac{\partial p}{\partial y} - \frac{\mu_l}{K} \frac{\rho}{\rho_l}(v - v_s) - \frac{C\rho^2}{K^{1/2}\rho_l}|v - v_s|(v - v_s) - \nabla \cdot \left(\rho f_s f_l \vec{\boldsymbol{V}}_r v_r\right) + \vec{\boldsymbol{J}} \times \vec{\boldsymbol{B}}|_y \tag{3}$$

$$\frac{\partial}{\partial t}(\rho w) + \nabla \cdot (\rho \vec{\boldsymbol{V}} w) = \nabla \cdot \left(\mu_l \frac{\rho}{\rho_l} \nabla w\right) - \frac{\partial p}{\partial z} - \frac{\mu_l}{K} \frac{\rho}{\rho_l}(w - w_s) - \frac{C\rho^2}{K^{1/2}\rho_l}|w - w_s|(w - w_s) - \nabla \cdot (\rho f_s f_l \vec{\boldsymbol{V}}_r w_r) + \rho g + \rho g(\beta_T(T - T_0) + \beta_s(f_l^{\alpha} - f_{l,0}^{\alpha})) + \vec{\boldsymbol{J}} \times \vec{\boldsymbol{B}}|_z \quad (4)$$

where u, v, and w are the velocities in the x, y, and z directions, respectively, and $\vec{\boldsymbol{V}}_r = \vec{\boldsymbol{V}}_l - \vec{\boldsymbol{V}}_s$ is the relative velocity vector between the liquid phase and the solid phase. The subscripts s and l refer to the solid and liquid phases, respectively; p is the pressure; μ is the dynamic viscosity; f is the mass fraction; K is the permeability, a measure of the ease with which fluids pass through the porous mushy zone; C is the inertial coefficient; β_T is the thermal expansion coefficient; g is the gravitational acceleration; T is the temperature; $\vec{\boldsymbol{B}}$ is the magnetic induction vector; $\vec{\boldsymbol{J}}$ is the current density vector; and the subscript 0 represents the initial condition.

Energy

$$\frac{\partial}{\partial t}(\rho h) + \nabla \cdot (\rho \vec{\boldsymbol{V}} h) = \nabla \cdot \left(\frac{k}{c_s} \nabla h\right) + \nabla \cdot \left(\frac{k}{c_s} \nabla (h_s - h)\right) - \nabla \cdot (\rho(\vec{\boldsymbol{V}} - \vec{\boldsymbol{V}}_s)(h_l - h)) \quad (5)$$

where h is the enthalpy, k is the thermal conductivity, and c is the specific heat.

The detailed descriptions of the terms in Eqs. (1)–(5) can be found in references [18, 21] and will not be repeated here. The solid/liquid phase-change is handled by the continuum formulation [25]. The third, fourth, and fifth terms in the right-hand side of Eqs. (2)–(4) vanish at the solid region because of $u = u_s = v = v_s = w = w_s = 0$, and $f_l = 0$ for the solid. In the liquid region, K goes to infinity and all these terms also vanish [18, 21]. Those terms are only effective for the mushy zone, where $0 < f_l < 1$ and $0 < f_s < 1$. Therefore, the liquid region, mushy zone, and solid region can be handled by the same equations. During the fusion and solidification process, latent heat is absorbed or released in the mushy zone. By the use of enthalpy in Eq. (5), conduction in the solid region, and conduction and convection in the liquid region and mushy zone, the absorption and release of latent heat are all handled in the same equation.

2.2. Tracking of Free Surfaces

The volume-of-fluid (VOF) technique [24] was employed to track the dynamic free surfaces. The fluid configuration is defined by a volume of fluid function, $F(x, y, z, t)$, which represents the volume of liquid metal per unit volume and satisfies the following conservation equation.

$$\frac{dF}{dt} = \frac{\partial F}{\partial t} + (\vec{\boldsymbol{V}} \cdot \nabla)F = 0 \quad (6)$$

When averaged over the cells of a computing mesh, the average value of F in a cell is equal to the fractional volume of the cell occupied by fluid. A unit value of

F corresponds to a cell full of fluid, whereas a zero value indicates a cell contains no fluid. Cells with F values between zero and one are partially filled with fluid and identified as surface cells.

2.3. Boundary Conditions

The boundary conditions for the previous Eqs. (1)–(5) are given below.

2.3.1. Normal to the local free surface. For cells containing a free surface, that is, cells that contain fluid but have one or more empty neighbors, the following pressure conditions must be satisfied [24].

$$p = p_v + \gamma\kappa \tag{7}$$

where p is the pressure at the free surface in a directional normal to the local free surface and p_v is the plasma arc pressure, which is assumed to have a radial distribution in the following form [12].

$$p_v = P_{\max} \exp\left(-\frac{r^2}{2\sigma_p^2}\right) \tag{8}$$

where $P_{\max}$ is the maximum arc pressure at the arc center, which is calculated from the welding current [12], r is the distance from the arc center, and σ_p is the arc pressure distribution parameter [12]. κ in Eq. (7) is the free surface curvature given by

$$\kappa = -\left[\nabla \cdot \left(\frac{\vec{n}}{|\vec{n}|}\right)\right] = \frac{1}{|\vec{n}|}\left[\left(\frac{\vec{n}}{|\vec{n}|} \cdot \nabla\right)|\vec{n}| - (\nabla \cdot \vec{n})\right] \tag{9}$$

where $\vec{n}$ is the normal vector to the local surface, which is the gradient of VOF function $\vec{n} = \nabla F$.

2.3.2. Tangential to the local free surface. The Marangoni shear stress at the free surface in a direction tangential to the local free surface is given by

$$\tau_{\vec{s}} = \mu_l \frac{\partial\left(\vec{V} \cdot \vec{s}\right)}{\partial \vec{n}} = \frac{\partial\gamma}{\partial T}\frac{\partial T}{\partial \vec{s}} \tag{10}$$

where $\vec{s}$ is the local surface tangential vector. Since there is no surface tension coefficient data available for 6005-T4, the property of pure aluminum was used instead. For pure aluminum, surface tension coefficient γ is a function of temperature [26].

$$\gamma = 868 - 0.152(T - T_l) \tag{11}$$

where T is the temperature and T_l is the melting temperature of aluminum.

2.3.3. Top surface. At the arc center, in addition to droplet impingement, arc heat flux is also impacting on the base metal. Since the arc heat flux is relatively

concentrated, it is assumed that the heat flux is perpendicular to the base metal (i.e., neglecting the inclination of current and heat flux). Therefore, the temperature boundary conditions at the top surface of the base metal are

$$k\frac{\partial T}{\partial z}=\frac{\eta(1-\eta_d)Iu_w}{2\pi\sigma_q^2}\exp\left(-\frac{r^2}{2\sigma_q^2}\right)-q_{\text{conv}}-q_{\text{radi}}-q_{\text{evap}} \tag{12}$$

where I is the welding current, η is the arc thermal efficiency, η_d is the ratio of droplet thermal energy to the total arc energy, u_w is the arc voltage, and σ_q is the arc heat flux distribution parameter [18]. The heat loss due to convection, radiation, and evaporation can be written as

$$q_{\text{conv}}=h_c(T-T_\infty),\quad q_{\text{radi}}=\sigma\varepsilon\left(T^4-T_\infty^4\right),\quad q_{\text{evap}}=WH_v \tag{13}$$

where h_c is the convective heat transfer coefficient [18], T_∞ is the room temperature, which is 293 K in this case, σ is Stephan-Boltzmann Constant, ε is the surface radiation emissivity [26], H_v is the latent heat for the liquid-vapor phase-change [22], and W is the melt mass evaporation rate [27].

2.3.4. Symmetrical $y=0$ plane.

$$\frac{\partial T}{\partial y}=0;\quad \frac{\partial u}{\partial y}=0;\quad v=0;\quad \frac{\partial w}{\partial y}=0 \tag{14}$$

2.3.5. Other surfaces.

$$-k\frac{\partial T}{\partial \vec{n}}=q_{\text{conv}}\quad u=0\quad v=0\quad w=0 \tag{15}$$

2.4. Electromagnetic Force

In Eqs. (2)–(4), there are three terms caused by the electromagnetic force $\vec{J}\times\vec{B}$ which should be calculated first before the calculation of velocity. Assuming the electric field is a quasi-steady-state and the electrical conductivity is constant, the scalar electric potential, ϕ, satisfies the following Maxwell equation [21] in the local r-z coordinate system.

$$\nabla^2\phi=\frac{1}{r}\frac{\partial}{\partial r}\left(r\frac{\partial\phi}{\partial r}\right)+\frac{\partial^2\phi}{\partial z^2}=0 \tag{16}$$

The required boundary conditions for the solution of Eq. (16) are

$$-\sigma_e\frac{\partial\phi}{\partial z}=\frac{I}{2\pi\sigma_c^2}\times\exp\left(-\frac{r^2}{2\sigma_c^2}\right)\quad\text{at the top free surface} \tag{17}$$

$$\frac{\partial \phi}{\partial z} = 0 \quad \text{at } z = 0 \tag{18}$$

$$\frac{\partial \phi}{\partial r} = 0 \quad \text{at } r = 0 \tag{19}$$

$$\phi = 0 \quad \text{at } r = 10\sigma_c \tag{20}$$

where σ_e is the electrical conductivity and σ_c is the arc current distribution parameter [21]. From the distribution of electrical potential, the current density in the r and z directions can be calculated via

$$J_r = -\sigma_e \frac{\partial \phi}{\partial r} \quad J_z = -\sigma_e \frac{\partial \phi}{\partial z} \tag{21}$$

The self-induced azimuthal magnetic field is derived from Ampere's law [21].

$$B_0 = \frac{\mu_0}{r} \int_0^r J_z \, r dr \tag{22}$$

where μ_0 is the magnetic permeability in free space. Finally, the three components of electromagnetic force in Eqs. (2)–(4) are calculated via the following equations [22].

$$\vec{\boldsymbol{J}} \times \vec{\boldsymbol{B}}|_x = -B_\theta J_z \frac{x - x_a}{r} \quad \vec{\boldsymbol{J}} \times \vec{\boldsymbol{B}}|_y = -B_\theta J_z \frac{y}{r} \quad \vec{\boldsymbol{J}} \times \vec{\boldsymbol{B}}|_z = B_\theta J_r \tag{23}$$

2.5. Numerical Considerations

The governing equations were solved iteratively at each time step using the finite-volume method [28]. At each time step, the continuity and momentum equations were solved iteratively with a two-step projection method involving the time discretization of the momentum equations to get the velocity and pressure distributions [22]. Then, the energy equation was solved explicitly to obtain the enthalpy and temperature field. The species equation was solved in a similar way. This process was repeated for each iteration step. Iteration within a time step was terminated when the solutions of velocity, pressure, temperature, and species distributions converged. Then the VOF function equation was solved to obtain the new free surface and liquid pool domain. The temperature-dependent material properties were updated. The time step was then advanced and the above procedure was repeated until the desired time was reached.

Since the governing equations are valid for the entire computational domain including the liquid phase, the solid phase, and the mushy zone, there is no need to track the shape and extent of each phase. Therefore, a fixed grid system was used in the calculation with refined grid cells in the weld pool zone to improve accuracy. Due to the symmetry of the x-z plane of the domain, a grid system of $408 \times 66 \times 56$ points was used for the half computational domain to save the computational time. The finer grids concentrating on and around the weld pool move with the weld pool as the welding proceeds. Time step length varied during the calculation to ensure the

convergence and save computational time. The computation was performed on the Dell Precision 650® workstations with 3.2 GHz Pentium® 4 processors. It took about 71 hours of CPU time to simulate 1.4 s of real-time welding. The average time step is around 2×10^{-5} s.

3. EXPERIMENTS

The experimental setup is shown in Figure 2. In the experiments, bead-on-plate welds were made on aluminum alloy 6005-T4 plates 203.2 mm × 38.1 mm × 5 mm in dimension, which were extruded by Hydro Raufoss Automotive. Every weld coupon was chemically cleaned and degreased. The electrode material was 4043 produced by Alcoa. The diameter of the electrode wire was 1.6 mm in all experiments. The welding machine was a Lincoln PowerWave 455® programmable waveform controlled welding machine made by Lincoln Electric. The weld torch was fixed onto a small cart on a rail. Argon of 40 CFH was used as the shielding gas. To provide an adequate protection of the weld pool, a welding gun leading angle of 15° was used in the experiments. Although constant voltage power sources are more commonly employed in industry, a constant current power source is chosen to study the current effect on penetration. The weld bead was made at the center of the plate along the x direction, as shown in Figure 2. All welds started from 30 mm to the left end of the weld coupon. Before welding, the upper surface of the plate was brushed with a stainless steel brush to remove the oxide layer. Three major parameters could be adjusted during the process: welding current, wire feed speed, and arc/cart travel speed. Arc voltage was automatically set by the machine once other parameters were fixed. The experiments were closely monitored during the process by connecting the port on the PowerWave455® front panel to the serial port of a computer and using WaveDesigner® software from Lincoln Electric. The welding parameters, such as arc current, voltage, and welding time, were stored in the computer and put into the mathematical model.

Welded samples were sectioned, grinded, polished, and then etched for metallurgical characterizations. Macroscopic analysis was performed under stereoscopes and optical microscopes. An image acquisition system including a digital camera and a computer was used to capture and store the images. The weld penetration, width, and reinforcement were measured. Knoop hardness measurements were performed on the cross-sections of weld samples using a load of 100 g.

4. RESULTS AND DISCUSSION

4.1. Cold Weld

The formation of the cold weld for a GMAW of 6005-T4 aluminum alloy was calculated. The fluid flow pattern, temperature distribution, and the final weld bead shape were obtained. The welding conditions and material properties of both base metal and droplets used in the computation of cold weld are summarized in Tables 1 and 2. Droplet size, frequency, droplet impingement velocity, and temperature were selected for the current welding parameters according to the previous studies of droplet formation and acceleration under the effect of arc plasma. Simulation

Table 1. Thermophysical properties and welding conditions of cold weld used in the model

Property	Symbol	Value (unit)
Specific heat of solid phase	c_s	900* (J/kg · K)
Specific heat of liquid phase	c_l	900* (J/kg · K)
Thermal conductivity of solid phase	k_s	167** (W/m · K)
Thermal conductivity of liquid phase	k_l	167** (W/m · K)
Density of solid phase	ρ_s	2700** (kg/m^3)
Density of liquid phase	ρ_l	2300** (kg/m^3)
Coefficient of thermal expansion	β_T	2.34×10^{-5}** (/K)
Radiation emissivity	ε	0.4
Dynamic viscosity	μ_l	0.0012* (kg/m · s)
Heat of fusion	H	3.97×10^{5}* (J/kg)
Heat of vaporization	H_v	1.08×10^{7}* (J/kg)
Solidus temperature	T_s	880** (K)
Liquidus temperature	T_l	927** (K)
Ambient temperature	T_∞	293 (K)
Convective heat transfer coefficient	h_c	80 (W/m^2 · s)
Electrical conductivity	σ_e	2.5×10^{7}** (Ω^{-1} m^{-1})
Welding voltage	u_w	23.5 (V)
Welding current	I	183 (A)
Arc heat flux distribution parameter	σ_q	2.50×10^{-3} (m)
Arc current distribution parameter	σ_c	2.50×10^{-3} (m)
Welding speed	V_a	14.8 (m m s^{-1})
Arc thermal efficiency	η	60%
Ratio of droplet thermal energy to total arc energy	η_d	20%
Thickness of base metal	H_b	5.0 (mm)
Width of base metal	W_b	38.1 (mm)
Length of base metal	L_b	203.2 (mm)
Initial base metal temperature	T_b	293 (K)
Electrode wire diameter	d_w	1.60 (mm)
Electrode wire feed speed	V_w	69.8 (cm/s)
Droplet diameter	D_d	1.0 (mm)
Droplet generation frequency	F_d	268 (Hz)
Droplet impinging velocity	V_d	50 cm/s
Initial droplet temperature	T_d	1050 (K)
Maximum plasma arc pressure	$P_{\max}$	200 (Pa)
Plasma arc pressure distribution parameter	σ_p	5.0×10^{-3} (m)

*Property of pure aluminum [26].
**Property of 6005 [33].

Table 2. Welding parameters

	Time (t)	Current, amp	Voltage, volt	Wire feed speed, mm/s	Welding speed, mm/s
Cold	$t > 0$ s	183	23.5	69.8	14.8
Hot #1	$0 \text{ s} < t < 0.27$ s	225	23.5	84.6	14.8
	$t > 0.27$ s	183	23.5	69.8	14.8
Hot #2	$0 \text{ s} < t < 0.2$ s	183	23.5	69.8	0
	$t > 0.2$ s	183	23.5	69.8	14.8
Hot #3	$0 \text{ s} < t < 0.2$ s	183	23.5	69.8	−14.8
	$t > 0.2$ s	183	23.5	69.8	14.8

is started when the welding arc is ignited at 30 mm to the left edge of the plate. To simulate a realistic welding process where the weld torch has a 15° lead angle and to account for the moving speed of the welding arc, the droplet also has a horizontal velocity in the arc moving direction in addition to the vertical velocity.

Figure 3 shows a partial three-dimensional view of the simulated welding process at the very early state. Figure 4 is the side view of the initial stage of the welding process showing the weld bead shape change, temperature field, and velocity distribution, respectively.

At $t = 0.02$ s after the welding process was initiated, several droplets have impinged onto the workpiece plate. The bulk metal is still at a temperature close to the room temperature except for the area beneath and around the welding arc. The heat is conducted away very fast due to the high thermal conductivity of aluminum alloy and the liquid solidifies very quickly once it impinges onto the solid metal surface. At this moment, the heat provided by the additional several droplets and welding arc is neither enough to melt the base metal nor sufficient to re-melt the previously solidified material. Therefore, the droplets solidify and overlap with each other and a small hump is formed under the arc center. It is also observed that although the welding process starts at $x = 30$ mm in the figures, some material spreads out to the left side of the starting point.

As the welding proceeds, the arc center moves to the positive x direction. More droplets hit the base metal surface and more heat is inputted from the welding arc. The workpiece and previously formed hump are gradually heated up. From $t = 0.06$ s to $t = 0.14$ s, the top portion of the hump is melted and the liquid begins to spread out and the height of the hump is lowered. More metal is melted near the arc center because the arc heat flux is assumed to have a Gaussian distribution and impinging droplets also carry the energy into the molten pool.

As the welding process proceeds further, more heat accumulates in the welding area, the base metal plate is heated up further, more metal is melted, and the molten pool size grows. For example, from $t = 0.27$ s, there is enough heat to melt not only

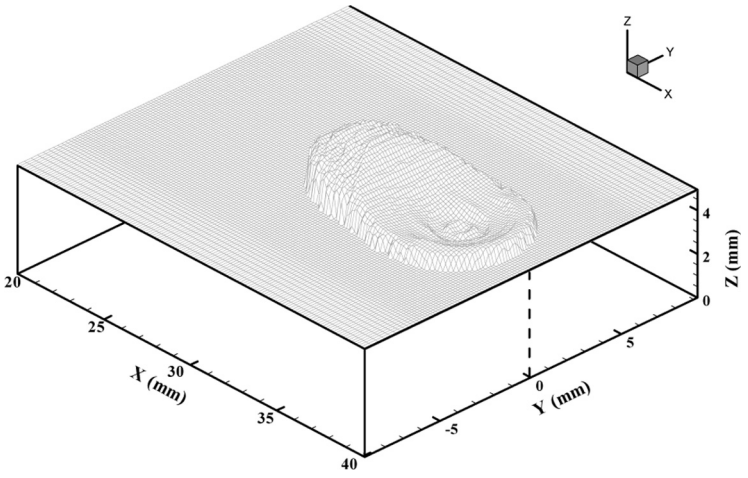

Figure 3. Partial three-dimensional view of the simulated weld.

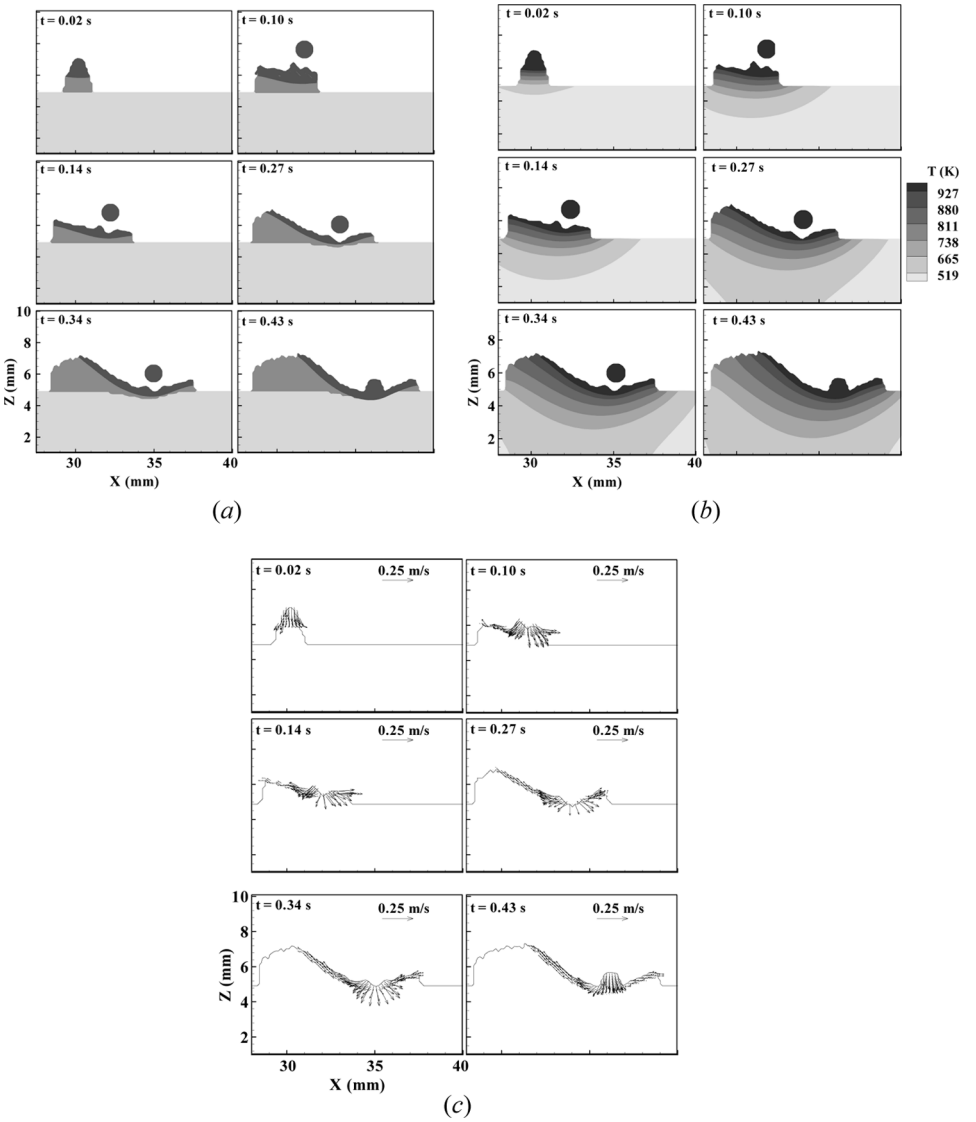

Figure 4. Side view of a cold weld formation. (*a*) Weld bead (the region with the darkest color is the weld pool, and the second darkest region is the weld bead), (*b*) temperature field, and (*c*) velocity field (droplets not shown).

the previously deposited material but also the base metal under it. The fluid in the weld pool flows away from the arc center in two directions, one in the welding direction and the other one toward the opposite direction. The fluid flows downward, and when reaching the bottom of the weld pool, the fluid to the left side of weld center flows to the left, then upwards along the solid-liquid boundary, and the fluid to the right side flows to the right. The velocity of fluid to the left side decreases as it flows uphill, and when reaching the tail edge of weld pool, the fluid solidifies and forms the

top surface of the weld bead. A weld pool with a crater shaped surface is formed due to this flow pattern. While the weld pool moves to the positive x direction with the arc center, it solidifies at the rear end and forms the weld bead.

Figure 5 illustrates the front view of the cross-sectional weld bead shape change, temperature field, and velocity distribution at the arc center, respectively. It can be observed that at the beginning of the welding process, since the heat input is not enough to melt the solid metal and the thermal diffusivity of aluminum alloy is very high, the deposited material solidifies and forms a welding spot on the base metal surface. As the welding process continues, the temperature of metal increases, which melts both the weld bead metal and the workpiece. The liquid flows downward and outward under the influence of the arc pressure and droplet impingement, and thus

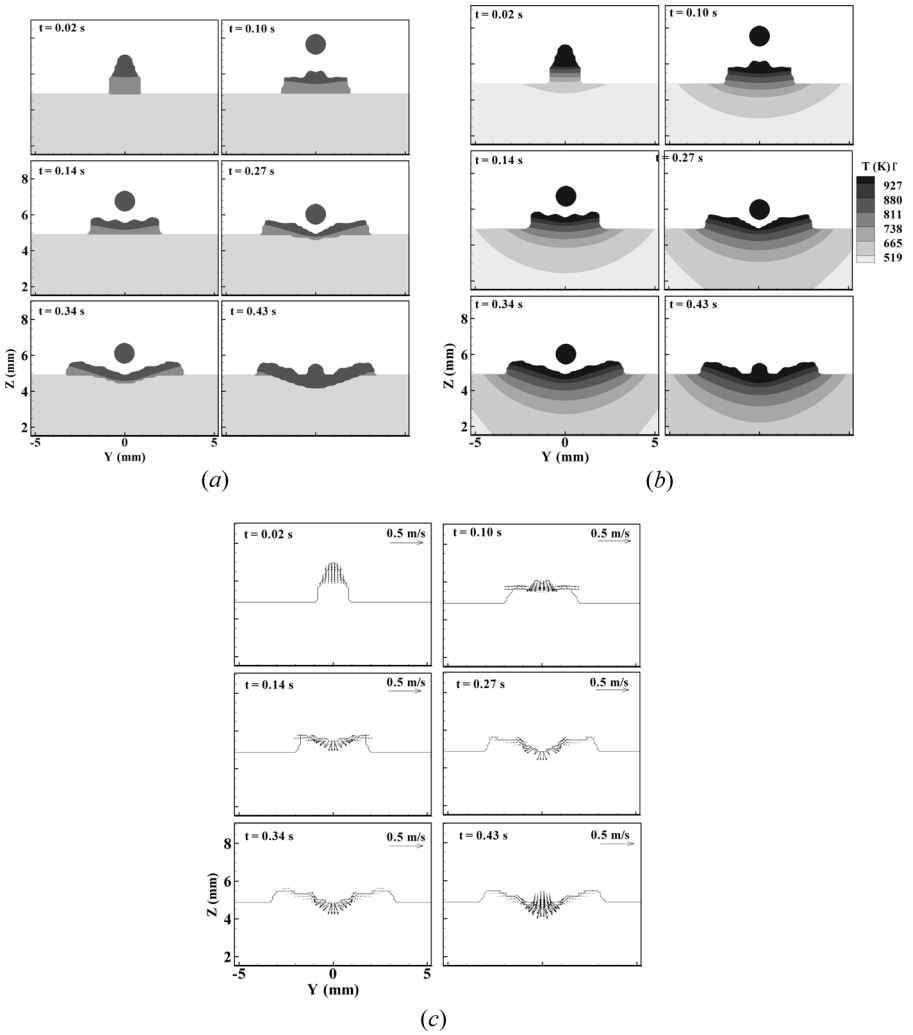

Figure 5. Corresponding front view of the weld formation, as shown in Figure 4.

spreads the melted metal to both sides of the weld. Therefore, the weld pool surface is depressed, penetration of the weld increases, and the weld pool becomes wider.

Figure 6 demonstrates the weld bead shape, temperature field, and velocity distribution at the cross-section of $x = 35\,\text{mm}$. At the beginning of the welding process, for example, when $t = 0.14\,\text{s}$, the weld pool has not reached $x = 35\,\text{mm}$. The base metal at the cross-section is heated up by heat conduction. As welding proceeds, the molten pool reaches $x = 35\,\text{mm}$ and liquid metal appears on this cross-section, showing similar shape and flow pattern to the cross-section at arc center. However, the outward flow from the center is not strong when the arc

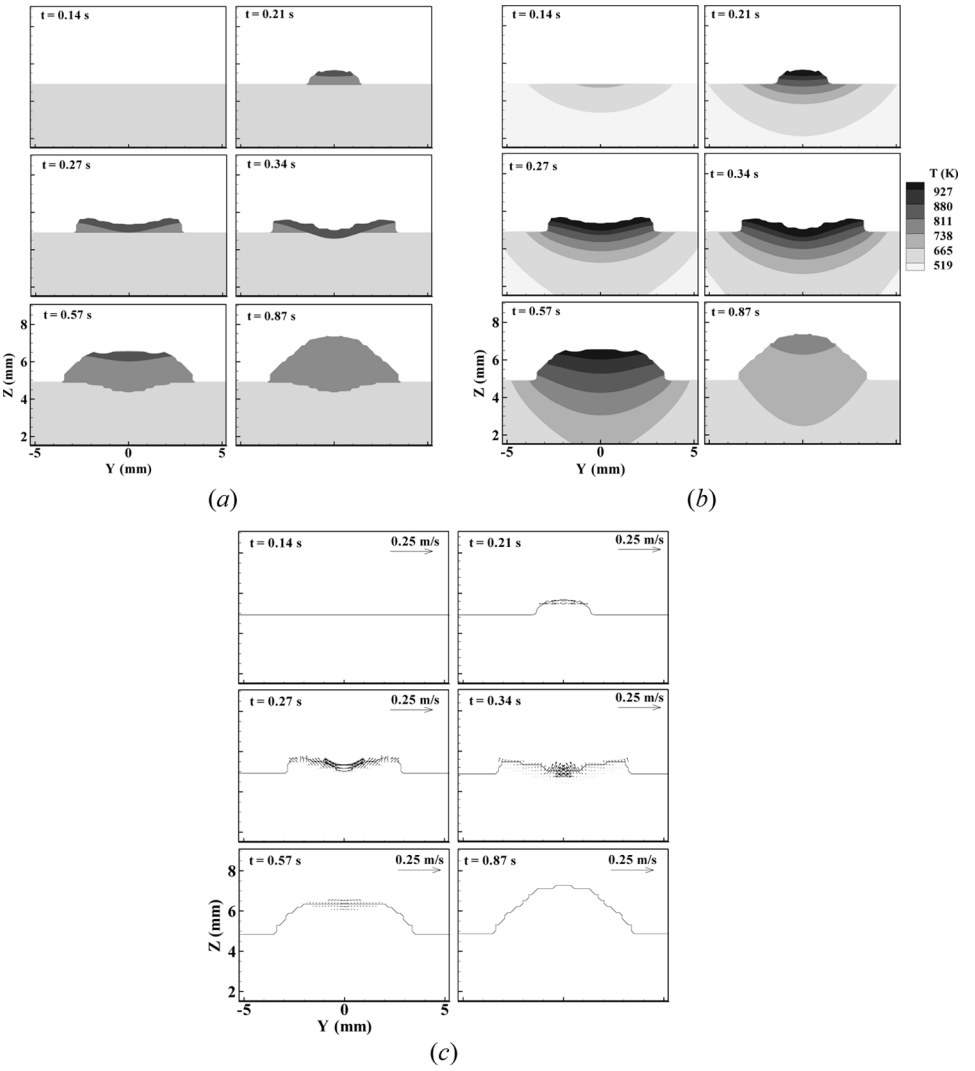

Figure 6. Corresponding cross-sectional view at $x = 35\,\text{mm}$ of the cold weld formation, as shown in Figure 4.

center is not at $x = 35$ mm. When the arc center is gradually approaching this position, the weld bead and molten pool become wider. After $t = 0.34$ s, the arc center moves past $x = 35$ mm cross-section and the amount of liquid metal decreases. At the same time, the weld bead area continues to grow. This is the result of fluid flowing uphill to the left side of the weld pool in Figure 4*a*. When the arc center moves further away, the temperature decreases and the molten metal solidifies and the weld bead is fully formed.

4.2. Hot Weld

It is usually desirable to increase the energy input at the beginning of welding to increase the penetration and suppress the formation of defects such as porosities. Three hot start techniques were used in this research. The hot start parameters are shown in Table 2. For Hot #1, faster wire feed speed and higher welding current (hot start parameters) were used at the initial stage of the welding process, and after 0.27 s the welding condition was switched back to the normal parameters. The actual variation of welding current is obtained by online monitoring of the welding and is shown in Figure 7. For Hot #2, the welding arc stayed at the original position for 0.2 s after ignition and then moved towards the welding direction. For Hot #3, the welding arc was started at $x = 33$ mm and moved backwards to the left side. Once it arrived at $x = 30$ mm, the moving direction was flipped to the right. The other parameters used in Hot #2 and Hot #3 were the same as the cold weld. The formation of hot welds was calculated. The fluid flow pattern, temperature distribution, and the final weld bead shape were obtained.

Figure 8 shows the formation of the weld bead at the initial stage of the welding process. Compared with the cold weld, more material is deposited onto the base metal surface due to the higher wire feed speed and the metal is heated up faster and

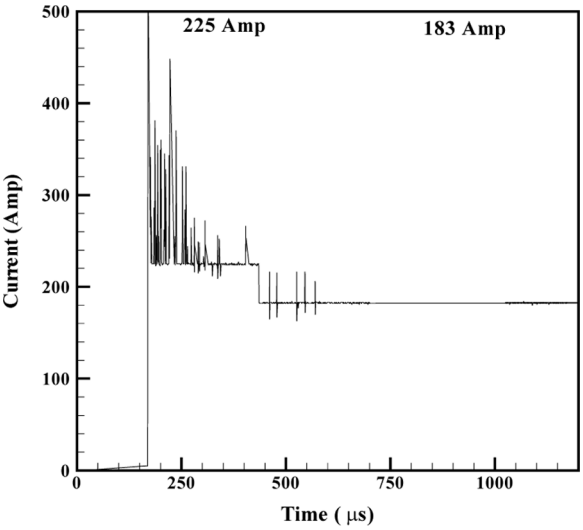

Figure 7. Welding current in hot start experiment Hot #1.

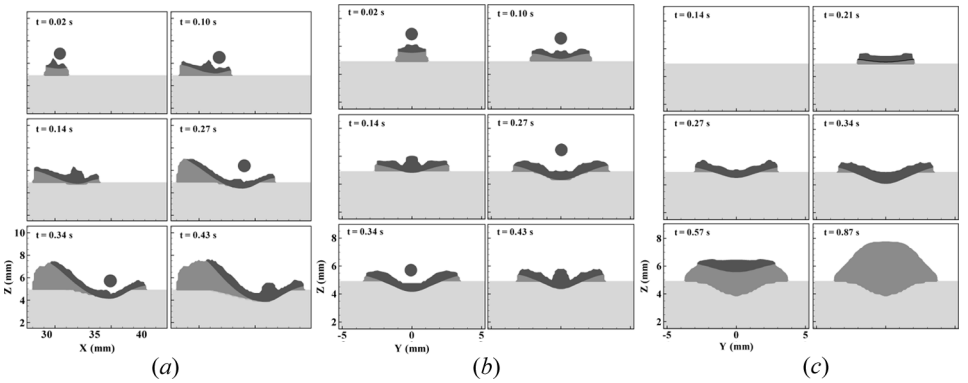

Figure 8. Weld formation of Hot #1 showing the weld bead. (*a*) Side view, (*b*) front view, and (*c*) cross-sectional view at $x = 35$ mm.

more material is melted as a result of higher heat input. At $t = 0.02$ s, the weld bead material begins to collapse and spread out on the surface, while in the cold weld the small hump is still building up. At $t = 0.14$ s, the base metal is melted by the heat flux provided by the transferred droplet and welding arc, while in the cold weld no base metal is melted. Similar to the cold weld, the fluid flow pattern in the weld pool is downward and outward from the arc center. Deeper penetration is obtained as a result of higher energy input. Due to the larger amount of material deposition, a larger weld bead is formed.

For Hot #2, the arc stays at the starting position $x = 30$ mm for 0.2 s then moves in the welding direction. Similar to the cold start, a hump is formed first at the arc center. When the enough number of successive droplets hit the same spot, the liquid metal collapses and spreads around under the effect of droplet impingement, surface tension, arc pressure, and gravity. After $t = 0.2$ s, the arc center moves to the right side, and the weld pool and weld bead are formed in a similar manner to the cold weld with increased penetration (Figure 9).

For Hot #3, the welding arc is started at $x = 3$ mm and goes backwards to the left side. After 0.2 s, it reaches $x = 30$ mm and the arc travel direction is switched to the positive x direction. When $t < 0.2$ s, the process is similar to the cold weld except that the arc moving direction is reversed, and therefore the temperature field and fluid flow are similar to the flipped picture of cold weld. Molten metal flows uphill to the right side and solidifies, forming a weld bead. After $t = 0.2$ s, the arc moves to the right side and the previously solidified weld bead metal is re-melted, becoming a portion of the weld pool liquid. The backward moving stage also serves as a pre-heating of the base metal. As the welding arc continues to move, a weld joint is formed with a deeper penetration compared with cold weld (Figure 10).

The very initial stage of welding is different for each of the four cases. For Hot #3, the welding arc moves backwards from its start position at $x = 33$ mm and then moves in the normal welding direction after 0.2 s. Therefore, it is informative to compare the final weld bead in the $x < 33$ mm region. The cross-sections at 32 mm are shown in Figure 11. It is clearly observed that the weld bead sizes of all the hot starts are much larger than those of the cold start because more electrode

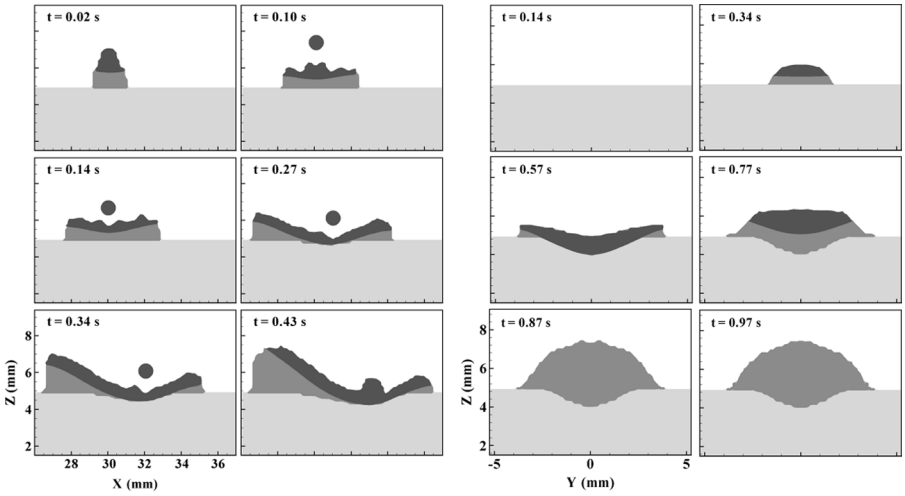

Figure 9. Weld formation of Hot #2 showing the weld bead. (*a*) Side view and (*b*) cross-sectional view at $x = 35\,\text{mm}$.

material is deposited on the base metal during this stage. The total volume of deposited metal is $19.0\,\text{mm}^3$ for cold start, $23.0\,\text{mm}^3$ for Hot #1, $47.0\,\text{mm}^3$ for Hot #2, and 37. $9\,\text{mm}^3$ for Hot #3. Comparing the results of the cold start and Hot #2 and #3, although the material deposition of the later two is twice as much as that of the former one, it is observed that the cross-section size area is clearly not twice as large. From the side of view of the weld bead formation (Figures 4*a*, 8*a*, 9*a*,

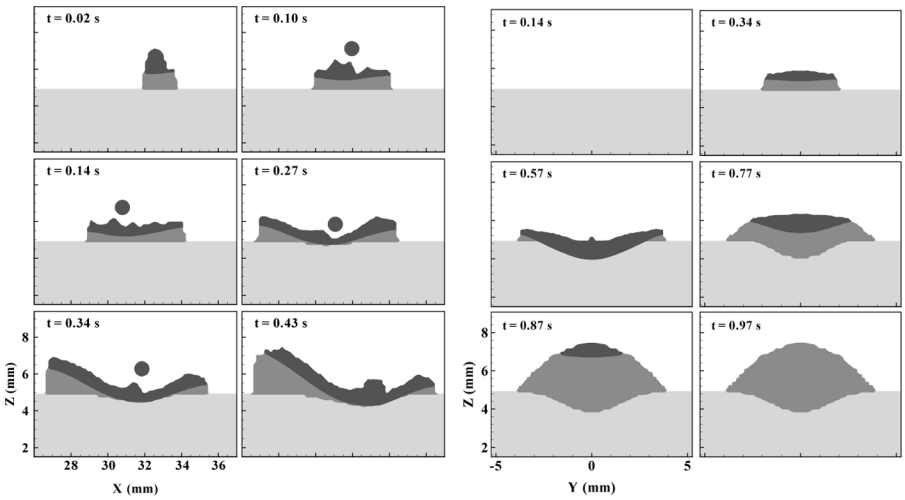

Figure 10. Weld formation of Hot #3 showing the weld bead. (*a*) Side view and (*b*) cross-sectional view at $x = 35\,\text{mm}$.

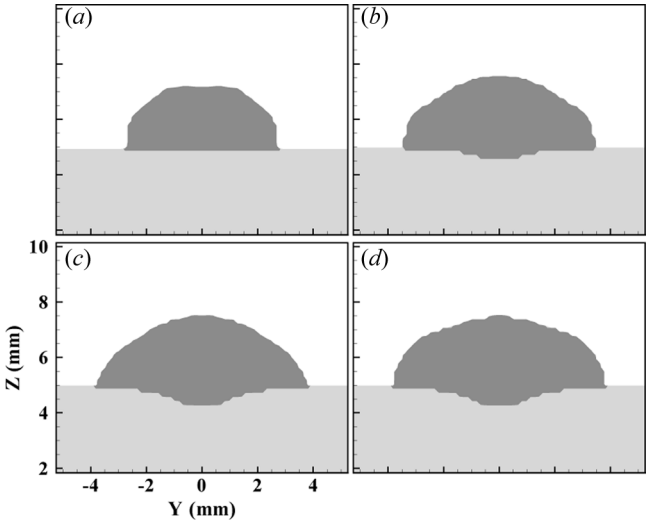

Figure 11. Cross-sectional view at $x = 32$ mm showing the weld beads. (*a*) Cold start, (*b*) Hot #1, (*c*) Hot #2, and (*d*) Hot #3.

and 10*a*), at the starting stage of welding, part of the weld bead material is pushed to the left-hand side. For the cold start, the furthest position of the weld bead can reach is about 1.55 mm to the left of the starting position; for Hot #1 it is about 2.0 mm; for Hot #2 it is 3.63 mm; and for #3 it is 3.39 mm. Therefore, the weld bead size is reduced from the hypothetical situation of no material being pushed to the left side of start position. The simulated weld bead dimensions of cross-section at $x = 35$ mm using three hot start techniques are shown in Table 3. All three techniques are able to improve the weld penetration to more than 200% of the cold weld value.

4.3. Experiment Validation

To validate the numerical model, experiments were performed for the cold weld and Hot #1. The base metal and resulting weld is shown in Figure 12.

Table 3. Dimensions of cross-sections at $x = 35$ mm

	Cold weld		Hot #1		Hot #2***	Hot #3***
	Experiment**	Simulation	Experiment**	Simulation	Simulation	Simulation
P*, mm	0.64	0.56	1.24	1.46	1.17	1.18
W*, mm	6.77	7.04	7.48	7.80	7.76	7.81
R*, mm	2.66	2.51	2.78	2.85	2.45	2.47

*P: penetration, W: width, and R: reinforcement.

**Average values are used for experimental results.

***For Hot #2 and Hot #3, only simulations were conducted. Hence, only simulated results are presented.

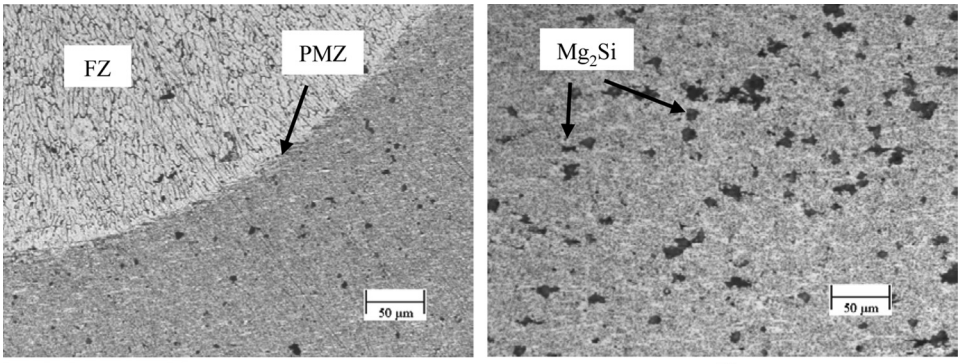

Figure 12. Zones near the fusion line at the cross-section of the weld. (*a*) Zones near the fusion line and (*b*) base metal.

The black zones in the base metal are Mg_2Si particles [29]. On the cross-section near the fusion line, the weld can be divided into three zones: fusion zone (FZ), where the metal was melted and then solidified; partial melted zone (PMZ), where the peak temperature was between the alloy's melting point and eutectic temperature; and heat-affected zone (HAZ), where no melting happened during welding but significant solid phase transformations took place. The FZ is characterized by columnar dendrites. The dark interdendritic network in the FZ is aluminum-silicon eutectic [29]. The PMZ has a coarse grain structure. In the HAZ near the weld bead, there are fewer Mg_2Si particles than in the base metal since, near the weld bead, the peak temperature is high enough for the particles to dissolve into the aluminum matrix. The cross-sections of the weld beads at $x = 35$ mm are compared with the simulated results in Figure 13 and Table 3. A good agreement between the experimental and calculated results was obtained.

Knoop micro-hardness measurements were conducted on the base metal and weld bead. The average hardness is HK 82.2 with a standard deviation of HK

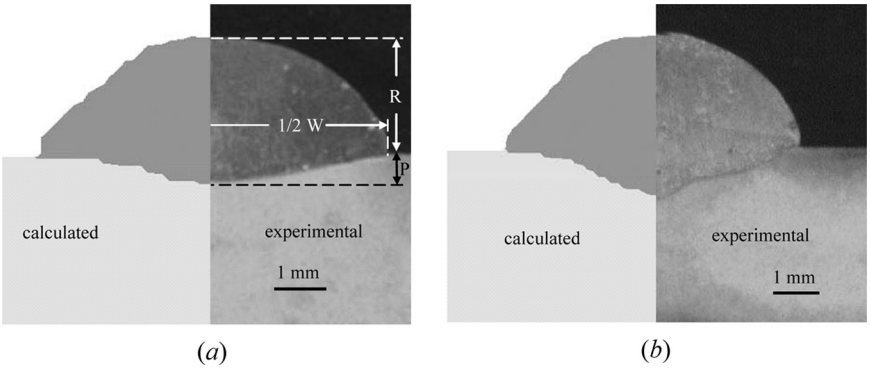

Figure 13. Comparison of the experimental and calculated results at $x = 35$ mm. (*a*) Cold weld and (*b*) Hot #1.

1.59 for the base metal and HK 54.3 with a standard deviation of HK 3.78 for the weld bead. Knoop hardness in the HAZ was measured on the $x = 35$ mm cross-section along a line 0.4 mm below the top surface of the welding sample (Figure 14*a*). The hardness profiles and the calculated peak temperature along the hardness measurement line are presented in Figure 14*b*. The 6005 alloy used in this research is a heat-treatable aluminum alloy, which gains its strength primarily through the formation of precipitates in the aluminum matrix during heat treatment [30].

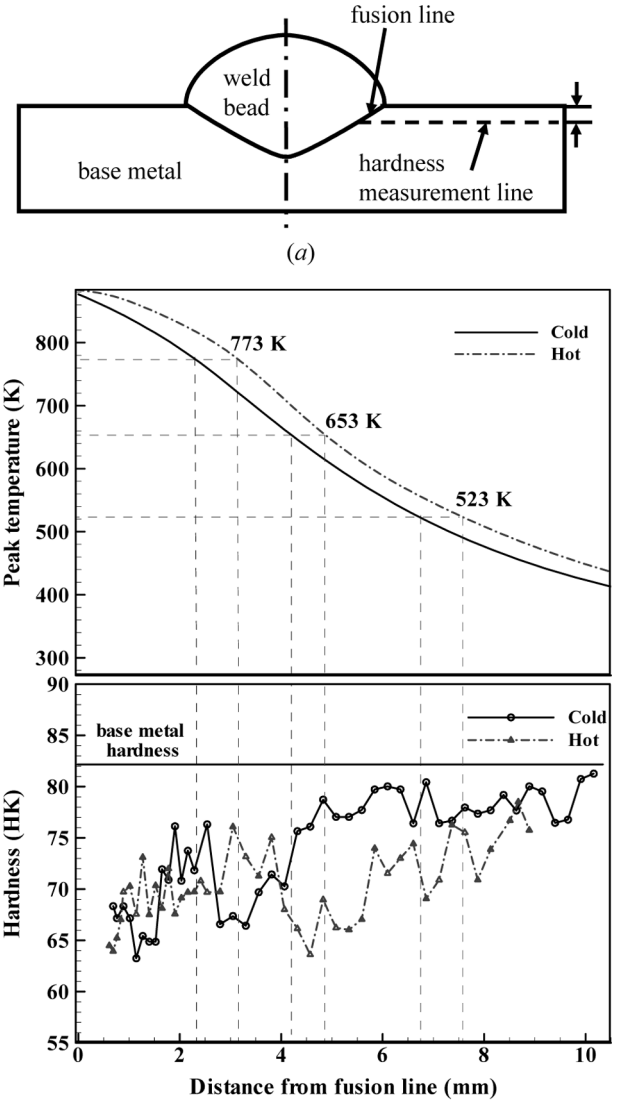

Figure 14. Knoop hardness measurement. (a) Measurement positions and (*b*) measurement results and peak temperature along the hardness measurement line on the cross-section at $x = 35$ mm.

When the peak temperature is below 523 K, the β″ phase coarsens in this zone, causing lower hardness than that of the base metal. When the peak temperature is in the range of 523 K and 653 K, the β″ phase continues to coarsen and also transforms to the β′ phase. At 653 K, the size of the β″ phase and the amount of the β′ phase reach the maximum and the strength of the metal decreases to a minimum value [31]. This corresponds to the lowest hardness. In the region where the temperature is between 653 K and 773 K, the dissolution of the β″ and β′ enriches the solid solution of the aluminum matrix with alloying element Mg [32]. Therefore, this zone may undergo a solution-hardening heat treatment during the heating and cooling of the welding process, which contributes to the rise of local hardness. When the temperature is higher than 773 K at a distance close to the fusion line, the hardness drops which might be caused by the diffusion of alloy element Mg between the solid and liquid metals at the interface between the weld pool and solid metal. Compared with the cold weld, the positions corresponding to temperatures 523 K, 653 K, and 773 K are 7.58 mm, 4.86 mm, and 3.16 mm from the fusion line, respectively, instead of 6.75 mm, 4.20 mm, and 2.33 mm. The wider high temperature zones led to a generally lower hardness in the hot weld since the coarsening of the β″ phase and its transformation to the β′ precipitates are more serious when held at higher temperatures for longer time. The hot weld hardness shows a similar trend to cold weld. However, softening of the HAZ is more serious for hot welds because of the increased energy input, which can be alleviated through heat treatment.

5. CONCLUSION

The fluid flow and heat and mass transfer in the weld pool for moving GMAW of aluminum alloy 6005 were analyzed. Weld pool and weld bead shapes, temperature field, and velocity distribution were obtained for the starting stage of a welding process. Experiments were conducted on the formation of the start end of the weld. Metallurgical characterizations together with micro-hardness measurements were performed. It was found that the base metal is heated up gradually during welding. Due to the fast heat conduction, the base metal is not melted at the very beginning of the process. The base metal begins to melt only when the work piece is heated up by the energy provided by the welding arc and molted droplet. Three methods were proposed to input more energy at the start of the weld process: 1) increase the welding current at the initial stage; 2) let the arc stay at the starting position at the initial stage, then move it to the normal welding direction; and 3) move the arc backwards initially, then move it forward. These hot start techniques heat up the base metal more quickly and hence improve the weld bead penetration significantly. More serious softening of the HAZ occurs when using hot start techniques.

REFERENCES

1. V. Ryazantsev, V. Fedoseev, and A. Savostikov, Hydrocarbon Hypothesis of Metallurgical Porosity when Welding Aluminium Alloys, *Welding Int.*, vol. 12, pp. 907–910, 1998.
2. G. Haynes and J. Bijendra, Joining Aluminum to Steel with Transition Material, *SAE Tech. Paper*, pp. 1999–01–0660, 1999.

3. O. Myhr, S. Klokkehaug, O. Grong, H. Fjaer, and A. Kluken, Modelling of Microstructure Evolution, Residual Stresses, and Distortions in 6082-T6 Aluminium Weldments, *Welding J.*, vol. 77, pp. 286s–292s, 1998.
4. P. B. Dickerson, Quality Control in Aluminum Arc Welding, *Proc. of the Aluminum Joining Seminar*, pp. 331–359, 1986.
5. O. Runnerstam and K. Persson, The Importance of a Good Quality Gas Shield, *Svetsaren*, vol. 50, pp. 25–27, 1995.
6. P. Dickerson and B. Irving, Welding Aluminum: It's Not as Difficult as it Sounds, *Welding J.*, vol. 71, pp. 44–50, 1992.
7. *Welding Aluminum: Theory and Practice*, 3rd ed., The Aluminum Association, 1997.
8. J. Hinchen, Avoiding Problems When Welding Aluminium, *Welding and Metal Fabrication*, vol. 56, pp. 132–138, 1988.
9. H. Cary, Welding Aluminum, *World of Welding*, vol. 11, pp. 11–16, 1998.
10. N. Andersen, Welded Aluminium Constructions on Rail, Road and Sea, *Svetsaren*, vol. 50, pp. 28–31, 1995.
11. W. Tong, Experimental Investigation of Welding Penetration-Depth in High-Purity Aluminum, *ASME HTD*, vol. 323, pp. 275–282, 1996.
12. M. Ushio and C. S. Wu, Mathematical Modeling of Three-Dimensional Heat and Fluid Flow in a Moving Gas Metal Arc Weld Pool, *Metal. and Mater. Trans. B*, vol. 28B, pp. 509–516, 1995.
13. W. H. Kim, H. G. Fan, and S. J. Na, Effect of Various Driving Forces on Heat and Mass Transfer in Arc Welding, *Numer. Heat Transfer A*, vol. 32, pp. 633–652, 1997.
14. H. Park and S. Rhee, Analysis of Weld Geometry Considering the Transferring Droplets in Gas Metal Arc Welding, *JSME Int. J., Series C*, vol. 44, pp. 856–862, 2001.
15. J. Jaidi and P. Dutta, Modeling of Transport Phenomena in a Gas Metal Arc Welding Process, *Numer. Heat Transfer A*, vol. 40, pp. 543–562, 2001.
16. M. H. Davies, M. Wahab, and M. J. Painter, An Investigation of the Interaction of a Molten Droplet with a Liquid Weld Pool Surface: A Computational, and Experimental Approach, *Welding J.*, vol. 79, pp. 18s–23s, 2000.
17. K. Mundra, T. DebRoy, and K. M. Kelkar, Numerical Prediction of Fluid Flow and Heat Transfer in Welding with a Moving Heat Source, *Numer. Heat Transfer A*, vol. 29, pp. 115–127, 1996.
18. Y. Wang and H. L. Tsai, Impingement of Filler Droplets and Weld Pool Dynamics during Gas Metal Arc Welding Process, *Int. J. Heat and Mass Transfer*, vol. 44, pp. 2067–2080, 2001.
19. H. G. Fan and R. Kovacevic, A Unified Model of Transport Phenomena in Gas Metal Arc Welding including Electrode, Arc Plasma and Molten Pool, *J. Phys. D: Appl. Phys.*, vol. 37, pp. 2531–2544, 2004.
20. J. Hu and H. L. Tsai, Heat and Mass Transfer in Gas Metal Arc Welding, Part II: The Metal, *Int. J. Heat Mass Transfer*, vol. 50, pp. 808–820, 2007.
21. J. Hu and H. L. Tsai, Modeling of Transport Phenomena in 3D GMAW of Thick Metal with V-Groove, *J. Phys. D: Appl. Phys.*, vol. 41, pp. 065202, 2008.
22. J. Hu, H. Guo, and H. L. Tsai, Weld Pool Dynamics and the Formation of Ripples in 3D Gas Metal Arc Welding, *Int. J. Heat Mass Transfer*, vol. 51, pp. 2537–2552, 2008.
23. V. K. Arghode, A. Kumar, S. Sundarraj, and P. Dutta, Computational Modeling of GMAW Process for Joining Dissimiliar Aluminum Alloys, *Numer. Heat Transfer A*, vol. 53, pp. 432–455, 2008.
24. D. B. Kothe, R. C. Mjolsness, and M. D. Torrey, *Ripple: A Computer Program for Incompressible Flows with Free Surfaces*, Los Alamos National Laboratory, 1991.
25. Q. Z. Diao and H. L. Tsai, Modeling of Solute Redistribution in the Mushy Zone during Solidification of Aluminum-Copper Alloys, *Metal. Trans. A*, vol. 24A, pp. 963–973, 1993.

26. J. E. Hatch, *Aluminum: Properties and Physical Metallurgy*, American Society for Metals, Metals Park, Ohio, 1984.
27. T. Zacharia, S. A. David, and J. M. Vitek, Effect of Evaporation and Temperature Dependent Material Properties on Weld Pool Development, *Metal. Trans. B*, vol. 22B, pp. 233–241, 1992.
28. S. V. Patankar, *Numerical Heat Transfer and Fluid Flow*, Hemisphere, New York, 1980.
29. G. F. Vander Voort, *Metallography and Microstructures*, vol. 9, 9th ed., American Society for Metals, Metals Park, Ohio, 1985.
30. H. Guo, J. Hu, and H. L. Tsai, Formation of Weld Crater in GMAW of Aluminum Alloys, *Int. J. Heat Mass Transfer*, vol. 52, pp. 5533–5546, 2009.
31. V. Malin, Study of Metallurgical Phenomena in the HAZ of 6061-T6 Aluminum Welded Joints, *Welding J.*, vol. 74, pp. 305s–318s, 1995.
32. S. D. Dumolt, Ph.D. Metallurgical Transformations in the Heat-Affected Zone of Aluminum Alloys by Transmission Electron Microscopy, Ph.D thesis, the Carnegie-Mellon University, Pittsburgh, Pennsylvania, 1983.
33. W. H. Cubberly, *Properties and Selection: Nonferrous Alloys and Pure Metals*, vol. 2, 9th ed., American Society for Metals, Metals Park, Ohio, 1985.